

# Computer Model Calibration Using High Dimensional Output

Dave Higdon, Los Alamos National Laboratory  
Jim Gattiker, Los Alamos National Laboratory  
Brian Williams, Los Alamos National Laboratory  
Maria Rightley, Los Alamos National Laboratory  
LA-UR-05-6410

This work focuses on combining observations from field experiments with detailed computer simulations of a physical process to carry out statistical inference. Of particular interest here is determining uncertainty in resulting predictions. This typically involves calibration of parameters in the computer simulator as well as accounting for inadequate physics in the simulator. The problem is complicated by the fact that simulation code is sufficiently demanding that only a limited number of simulations can be carried out. We consider applications in characterizing material properties for which the field data and the simulator output are highly multivariate. For example, the experimental data and simulation output may be an image or may describe the shape of a physical object. We make use of the basic framework of Kennedy and O’Hagan (2001). However, the size and multivariate nature of the data lead to computational challenges in implementing the framework. To overcome these challenges, we make use of basis representations (e.g. principal components) to reduce the dimensionality of the problem and speed up the computations required for exploring the posterior distribution. This methodology is applied to applications, both ongoing and historical, at Los Alamos National Laboratory.

Keywords: computer experiments; prediction; uncertainty quantification; Gaussian process; predictive science; functional data analysis

## 1 Introduction

Understanding and predicting the behavior of complex physical processes is crucial in a variety of applications that include weather forecasting, oil reservoir management, hydrology, and impact dynamics. Inference on such systems often makes use of computer code—a simulator—which simulates the physical process of interest along with field data collected from experiments or observations on the actual physical system. The simulators we work with at Los Alamos National Laboratory (LANL) typically model fairly well-understood physical processes—this can be contrasted with agent-based simulations, which model social activity. Even so, uncertainties play an important role in using the code to predict behavior of the physical system. Uncertainties arise from a variety of sources that include: uncertainty in the specification of initial conditions; uncertainty in the value of important physical constants (e.g. melting temperatures, equations of state, stress-strain rates); inadequate mathematical models in the code to describe physical behavior; and inadequacies in the numerical algorithms used for solving the specified mathematical systems (e.g. unresolved grids).

The features above clearly distinguish the simulation code from the actual physical system of interest. However much of this uncertainty can be mitigated by utilizing experimental observations to constrain uncertainties within the simulator. When the simulation code is sufficiently fast, estimation approaches based on Monte Carlo can be used (Berliner, 2001; Higdon et al., 2003; Kaipio and Somersalo, 2004). In applications such as weather forecasting where both the data and simulations arrive in a sequential fashion, filtering approaches can also be quite useful (Bengtsson et al., 2003; Kao et al., 2004).

When the application is not readily amenable to sequential updating and the simulation code takes minutes, days, or even weeks to complete, alternative estimation approaches are required. This is the case for our applications. In this paper we base our approach on that of Kennedy and O’Hagan (2001) which utilizes the Gaussian process (GP) models described in Sacks et al. (1989) to model the simulator output and untried input settings. This model for the simulator is then embedded in a larger framework so that parameter estimation (i.e. calibration) and prediction can be carried out. Section 2.1 gives a fully Bayesian overview of this formulation.

Although the formulation can, in principal, account for multivariate simulation and experimental output, even moderately multivariate output can render the required computations for fitting such models infeasible. Our experience is that multivariate output is quite common in physics and engineering applications. This paper describes an extension of this formulation that allows for highly multivariate output, while still maintaining sufficient computational tractability to allow a fully Bayesian analysis via Markov chain Monte Carlo (MCMC).

### 1.1 Historical implosion experiments

To facilitate the description of our methodology, we utilize an application from the beginnings of the Manhattan project at LANL (Neddermeyer, 1943) in which steel cylinders were imploded by a high explosive (HE) charge surrounding the cylinder. Figure 1 shows the results of such experiments.

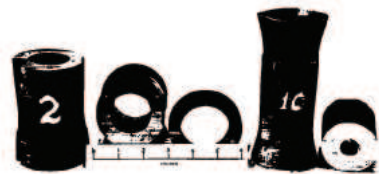


Figure 1: Cylinders before and after implosion using TNT. Photos are from Neddermeyer (1943) experiments 2 and 10.

To describe these implosions, Neddermeyer devised a rudimentary physical model to simulate an experiment which depends on three inputs:

- $x_1$ : the mass of HE used in the experiment;
- $t_1$ : detonation energy per unit mass of HE;
- $t_2$ : yield stress of steel.

The first input  $x_1$  is a condition under the control of the experimenter; the remaining two inputs  $\mathbf{t} = (t_1, t_2)$  hold parameter values. We wish to estimate the best setting  $\mathbf{t} = \boldsymbol{\theta}$  from the experimental data. More generally in the framework, we describe simulation inputs with the joint vector  $(\mathbf{x}, \mathbf{t})$  where the  $p_x$ -vector  $\mathbf{x}$  denotes controllable—or at least observable—input conditions of the experiment, and the  $p_t$ -vector  $\mathbf{t}$  holds parameter values to be calibrated, or estimated. Hence, a given simulation is controlled by a  $(p_x + p_t)$ -vector  $(\mathbf{x}, \mathbf{t})$ , which contains the input settings. In this cylinder example we have  $p_x = 1$  and  $p_t = 2$ .

Output from Neddermeyer’s simulation model for a particular input setting  $(\mathbf{x}, \mathbf{t})$  is shown in Figure 2. In describing the modeling formulation, we will need to make the distinction between an arbitrary setting  $\mathbf{t}$  for the calibration inputs, and the true setting  $\boldsymbol{\theta}$ , which is something we are

trying to estimate. While this particular simulation code runs very quickly, we mean it to be a placeholder for a more complicated, and computationally demanding, code from which a limited number of simulations (typically less than 200) will be available for the eventual analysis.

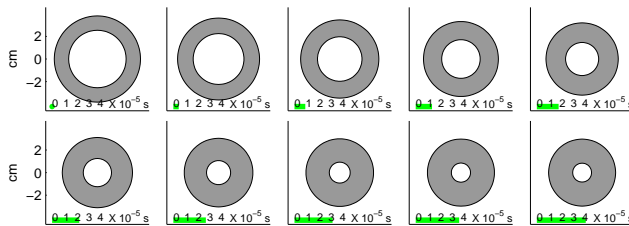


Figure 2: Evolution of the implosion of the steel cylinder using Neddermeyer's simulation model.

The data from this application come in the form of a sequence of high-speed photographs taken during the implosion, which takes place over a span of about 30 microseconds. The original photographs from the experiments were unavailable so we construct synthetic data using the rudimentary simulation model using a true value of  $\theta = (\frac{1}{2}, \frac{1}{2})$  for the calibration parameters. We generated data from three experiments, each with different values for  $x_1$ , the HE mass. For experiments 1, 2, and 3  $x_1$  is .77, .05, and .96 respectively, in standardized units. To better mimic reality, we also add an effect to this synthetic data that results in slightly faster inward movement of the inner radius at angles  $\phi$  between the detonators which are at  $\phi = 0^\circ, 90^\circ, 180^\circ$ , and  $270^\circ$ . This effect is due to colliding detonation waves induced by the four separate detonations. This effect varies with  $\phi$  and is therefore not accounted for in the simulation model which assumes the radius is constant over  $\phi$  at any given time. The experimental data are shown in Figure 3. As is typical of experiments we are involved in, the amount and condition of the observed data varies with experiment. Here the number of photographs and their timing varies with experiment. We take a trace of the inner radius of the cylinder to be the response of interest. The trace, described by angle  $\phi$  and radius  $r$ , consists of 16 points equally spaced by angle.

We choose this example as the context in which to explain our approach because it possesses the features of the applications we are interested in, while still remaining quite simple. Specifically, we point the reader to the following properties of this example:

- The application involves a simulator from which only a limited number of simulations  $m$  ( $m < 200$ ) may be carried out. Simulator output depends on a vector of input values  $(\mathbf{x}, \mathbf{t})$  where the  $p_x$ -vector  $\mathbf{x}$  denotes the input specifications and the  $p_t$ -vector  $\mathbf{t}$  holds parameter settings to be calibrated.
- The dimensionality of the input vector  $(\mathbf{x}, \mathbf{t})$  is limited. Here it is a three-dimensional vector ( $p_x + p_t = 1 + 2 = 3$ ); in the application of Section 3,  $p_t = 8$ . We have worked with applications for which the dimension of  $(\mathbf{x}, \mathbf{t})$  is as large as 60. However applications with high-dimensional ( $p_t > 100$ ) inputs, as is the case in inverse problems and tomography applications, are beyond the scope of the approach given here.
- Observations from one or more experiments are available to constrain the uncertainty regarding the calibration parameter  $\theta$ . In most applications we have worked with, the number of experiments  $n$  is small ( $n < 10$ ). The experimental data are typically collected at various input conditions  $\mathbf{x}$ , and the simulator produces output that is directly comparable to these

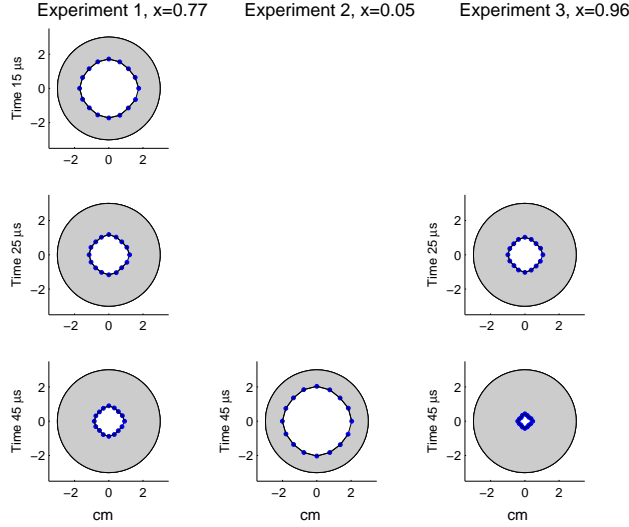


Figure 3: Hypothetical data obtained from photos at different times during the 3 experimental implosions. All cylinders initially had a 1.5 in outer and a 1.0 in inner radius.



Figure 4: A modern implosion experiment carried out at the dual axis radiographic hydrodynamic test facility at LANL. High energy x-rays interrogate the object as it implodes.

field observations. Note that the simulator can also model the observation process used in the experiment to ensure that the simulations are compatible with the experimental data.

The goal of the analysis described in the next section is to:

- use the experimental data to constrain the uncertainty regarding the calibration parameters  $\theta$ ;
- make predictions (with uncertainty) at new input conditions  $\mathbf{x}$ ; and
- estimate systematic discrepancies between the simulator and physical reality.

We develop our methodology in the context of Neddermeyer’s implosion application. We currently apply this methodology to modern implosion experiments conducted at the dual axis hydrodynamic radiographic tomography facility at LANL which uses high energy x-rays to record the implosion (Figure 4). Current simulation models are also far more advanced, with detailed models for material properties and equations of state. Even using the most modern supercomputers, these simulations can take hours, or even days.

Although the focus here is on implosion experiments, the methodology readily generalizes to other applications. In the following section we describe the basic, univariate model formulation, and then give our extension to deal with highly multivariate data. In Section 3, we apply this

methodology to a modern cylinder test for high explosives. The paper then concludes with a discussion.

## 2 Model Formulation

In this section we review the basic univariate formulation of Kennedy and O’Hagan (2001). Theirs is a methodology for calibrating a computationally demanding simulator that may be biased when compared to reality. After pointing out difficulties with directly applying this formulation when the simulation and experimental output is highly multivariate, we describe the details of our extension of this methodology. Throughout this section, we use Neddermeyer’s cylinder application to motivate the model formulation.

### 2.1 Univariate formulation

Here we give a brief explanation of the univariate formulation of Kennedy and O’Hagan (2001). Although their original implementation is not fully Bayesian, we give a fully Bayesian description here since it better integrates with the multivariate formulation to follow. The formulation is described in general and then followed by an application to one of the Neddermeyer experiments.

At various settings  $\mathbf{x}_1, \dots, \mathbf{x}_n$ , observations  $y_1, \dots, y_n$  are made of the physical system

$$y(\mathbf{x}_i) = \zeta(\mathbf{x}_i) + \epsilon(\mathbf{x}_i), \quad i = 1, \dots, n,$$

where  $\zeta(\mathbf{x}_i)$  denotes the response of the actual physical system and the  $\epsilon(\mathbf{x}_i)$ ’s denote observation error. In one of these cylinder experiments,  $\zeta(\mathbf{x}_i)$  represents the actual radius of the cylinder as a function of  $\mathbf{x}_i$ , which encodes the amount of HE, angle, and time;  $y(\mathbf{x}_i)$  gives the experimentally observed radius at  $\mathbf{x}_i$ . Often the size and nature of the  $\epsilon(\mathbf{x}_i)$ ’s are sufficiently well characterized that their distribution can be treated as known. We take  $\mathbf{y} = (y(\mathbf{x}_1), \dots, y(\mathbf{x}_n))^T$  to denote the physical observations. If the observations are multivariate,  $\mathbf{x}_i$  can be used to encode the elements of the observations. For the cylinder experiments, this could be accomplished by having  $\mathbf{x}_i$  index the time and angle of each observation. Hence a single experiment may account for many components of the vector  $\mathbf{y}$ .

The observed data are then modeled statistically using the simulator  $\eta(\mathbf{x}, \boldsymbol{\theta})$  at the best calibration value  $\boldsymbol{\theta}$  according to

$$y(\mathbf{x}_i) = \eta(\mathbf{x}_i, \boldsymbol{\theta}) + \delta(\mathbf{x}_i) + \epsilon(\mathbf{x}_i), \quad i = 1, \dots, n,$$

where the stochastic term  $\delta(\mathbf{x}_i)$  accounts for discrepancy between the simulator  $\eta(\mathbf{x}_i, \boldsymbol{\theta})$  and reality  $\zeta(\mathbf{x}_i)$ , and  $\boldsymbol{\theta}$  denotes the best, but unknown, setting for the calibration inputs  $\mathbf{t}$ . In some cases, the discrepancy term can be ignored; in other cases it plays a crucial role in the analysis.

We treat the fixed set of  $m$  simulation runs

$$\eta(\mathbf{x}_j^*, \mathbf{t}_j^*), \quad j = 1, \dots, m,$$

as supplementary data to be used in the analysis. We are in the situation where the computational demands of the simulation code are so large that only a fairly limited number of runs can be carried out. In this case, a GP model for  $\eta(\mathbf{x}, \mathbf{t})$  is required for input combinations  $(\mathbf{x}, \mathbf{t})$  at which the simulator has not been run.

Generally, if  $\mathbf{x}$  is a vector in  $R^{p_x}$  and  $\mathbf{t}$  a vector in  $R^{p_t}$ , then the function  $\eta(\cdot, \cdot)$  maps  $R^{p_x+p_t}$  to  $R$ . We utilize a Gaussian process to model this unknown function (O’Hagan, 1978; Sacks et al., 1989; Santner et al., 2003). A mean function  $\mu(\mathbf{x}, \mathbf{t})$  and covariance function  $\text{Cov}((\mathbf{x}, \mathbf{t}), (\mathbf{x}', \mathbf{t}'))$  are required to fully specify a GP prior model for  $\eta(\mathbf{x}, \mathbf{t})$ . Following Sacks et al. (1989) and Kennedy and O’Hagan (2001) we scale all inputs to the unit hypercube, take  $\mu(\mathbf{x}, \mathbf{t})$  to be a constant, and specify a product covariance having power exponential form

$$\begin{aligned} \text{Cov}((\mathbf{x}, \mathbf{t}), (\mathbf{x}', \mathbf{t}')) &= \frac{1}{\lambda_\eta} \prod_{k=1}^{p_x} \rho_{\eta k}^{4(x_k - x'_k)^2} \times \prod_{k=1}^{p_t} (\rho_{\eta, p_x+k})^{4(t_k - t'_k)^2} \\ &= \frac{1}{\lambda_\eta} R((\mathbf{x}, \mathbf{t}), (\mathbf{x}', \mathbf{t}'); \boldsymbol{\rho}_\eta), \end{aligned} \quad (1)$$

where the parameter  $\lambda_\eta$  controls the marginal precision of  $\eta(\cdot, \cdot)$ , and the  $(p_x+p_t)$ -vector  $\boldsymbol{\rho}_\eta$  controls the dependence strength in each of the component directions of  $\mathbf{x}$  and  $\mathbf{t}$ . This specification leads to a smooth, infinitely differentiable representation for  $\eta(\cdot, \cdot)$ . The parameter  $\rho_{\eta k}$  is the correlation between outputs evaluated at inputs that vary in only the  $k$ -th dimension by half their domain. We note that it is often useful to add a small white noise component to the covariance model (1) to account for small numerical fluctuations in the simulation. Such fluctuations can be caused by slight changes in adaptive meshing or tolerances induced by changes in the input settings.

The prior model formulation is completed by specifying independent priors for the parameters controlling  $\eta(\cdot, \cdot)$ :  $\pi(\mu)$ ,  $\pi(\lambda_\eta)$ , and  $\pi(\boldsymbol{\rho}_\eta)$ . This prior formulation is discussed in Section 2.2.

The discrepancy term  $\delta(\mathbf{x})$  accounts for inadequacies in the simulation model. Inadequacies are often due to missing physics or approximations built into the simulation model, leading to systematic differences between reality  $\zeta(\mathbf{x})$  and the calibrated simulation model  $\eta(\mathbf{x}, \boldsymbol{\theta})$ . For Neddermeyer’s mathematical simulation model, the assumptions of symmetry and incompressibility of steel will yield discrepancies with reality. Often these discrepancies persist as input condition varies. To account for this we specify a GP model for the discrepancy term  $\delta(\mathbf{x})$  with mean function of 0, and a covariance function of the form

$$\begin{aligned} \text{Cov}(\mathbf{x}, \mathbf{x}') &= \frac{1}{\lambda_\delta} \prod_{k=1}^p \rho_{\delta k}^{4(x_k - x'_k)^2} \\ &= \frac{1}{\lambda_\delta} R((\mathbf{x}, \mathbf{x}'); \boldsymbol{\rho}_\delta). \end{aligned} \quad (2)$$

The prior specification for the parameters governing the GP model for  $\delta(\cdot)$  requires we define  $\pi(\lambda_\delta)$  and  $\pi(\boldsymbol{\rho}_\delta)$  which depend on the known ability of the simulator to adequately model the physical system.

We define  $\mathbf{y} = (y(\mathbf{x}_1), \dots, y(\mathbf{x}_n))^T$  to be the vector of field observations and  $\boldsymbol{\eta} = (\eta(\mathbf{x}_1^*, \mathbf{t}_1^*), \dots, \eta(\mathbf{x}_m^*, \mathbf{t}_m^*))^T$  to be the simulation outcomes from the experimental design. We also define the joint  $(n+m)$ -vector  $\mathcal{D} = (\mathbf{y}^T, \boldsymbol{\eta}^T)^T$  with associated simulation input values  $(\mathbf{x}_1, \boldsymbol{\theta}), \dots, (\mathbf{x}_n, \boldsymbol{\theta})$  for its first  $n$  components and  $(\mathbf{x}_1^*, \mathbf{t}_1^*), \dots, (\mathbf{x}_m^*, \mathbf{t}_m^*)$  for its final  $m$  components. The sampling model, or likelihood, for the observed data  $\mathcal{D}$  is then

$$L(\mathcal{D}|\boldsymbol{\theta}, \mu, \lambda_\eta, \boldsymbol{\rho}_\eta, \lambda_\delta, \boldsymbol{\rho}_\delta, \boldsymbol{\Sigma}_y) \propto |\boldsymbol{\Sigma}_{\mathcal{D}}|^{-\frac{1}{2}} \exp \left\{ -\frac{1}{2} (\mathcal{D} - \mu \mathbf{1}_{m+n})^T \boldsymbol{\Sigma}_{\mathcal{D}}^{-1} (\mathcal{D} - \mu \mathbf{1}_{m+n}) \right\}, \quad (3)$$

where

$$\Sigma_{\mathcal{D}} = \Sigma_{\eta} + \begin{pmatrix} \Sigma_y + \Sigma_{\delta} & 0 \\ 0 & 0 \end{pmatrix},$$

$\Sigma_y$  is the  $n \times n$  observation covariance matrix,  $\Sigma_{\eta}$  is obtained by applying (1) to each pair of the  $n + m$  simulation input points corresponding to  $\mathcal{D}$ , and  $\Sigma_{\delta}$  is a  $n \times n$  matrix obtained by applying (2) to each pair of the  $n$  input settings  $\mathbf{x}_i$ ,  $i = 1, \dots, n$ , that correspond to the observed field data  $\mathbf{y}$ . Note that  $\Sigma_{\eta}$  depends on the experimental input conditions  $\mathbf{x}_i$ , the simulator input conditions  $(\mathbf{x}_j^*, \mathbf{t}_j^*)$ , and the parameter value  $\theta$ . Hence updating  $\theta$  affects  $\Sigma_{\eta}$  which means its determinant and a linear solve need to be recomputed to evaluate (3).

The resulting posterior density has the form

$$\begin{aligned} \pi(\theta, \mu, \lambda_{\eta}, \rho_{\eta}, \lambda_{\delta}, \rho_{\delta} | \mathcal{D}) &\propto \\ L(\mathcal{D} | \theta, \mu, \lambda_{\eta}, \rho_{\eta}, \lambda_{\delta}, \rho_{\delta}, \Sigma_y) &\times \pi(\mu) \times \pi(\lambda_{\eta}) \times \pi(\rho_{\eta}) \times \pi(\lambda_{\delta}) \times \pi(\rho_{\delta}) \end{aligned}$$

which can be explored via Markov chain Monte Carlo (MCMC). We use tuned, univariate random walk Metropolis and Hastings updates in our MCMC implementation (Metropolis et al., 1953; Besag et al., 1995).

In Figure 5 the univariate formulation is applied to a simplification of experiment 1, from Section 1.1. Here the radii measurements of experiment 1 are averaged radially, giving a single measured radius at three different times indexed by  $x$ . For these simulations, only the detonation energy  $t$  was varied—the amount of HE and the yield stress of steel were held fixed at their nominal values. Hence  $\eta(x, t)$  gives the simulated radius as a function of time  $x$  and input detonation energy  $t$ . Even though the simulation model produces a trace of radius by implosion time, we take only the  $m = 20$  values corresponding to the dots in the top row plots of Figure 5. Each of these “simulations” is really only a single point taken from a dense time series produced by the simulator.

From Figure 5 it is clear this analysis infers about a number of important quantities. Of key interest in almost any application are the posterior estimates for  $\eta(x, t)$  (Figure 5(c)), the calibration parameters  $\theta$ , the calibrated simulator  $\eta(x, \theta)$  (Figure 5(d)), the model discrepancy  $\delta(x)$  (Figure 5(e)), and the physical system  $\zeta(x)$  (Figure 5(f)). With these, one can explore the sensitivities of the simulator model, describe the parameter settings for which the simulator is consistent with the data, and make predictions for the physical system at settings  $x$  for which no experimental data exists.

## 2.2 Extension to multivariate formulation

This basic formulation has proven effective in a wide variety of applications—see Higdon et al. (2004) or Bayarri et al. (2005) for additional examples. However, the size of any problem one might tackle with this basic approach is limited since a likelihood (3) evaluation requires a solve of an  $(n + m) \times (n + m)$  matrix. This is painfully obvious in the imploding cylinder application of Section 1.1 where a single simulation produces a  $20 \times 26$  grid of radii over time and angle. Here the 36 simulations result in 18,720 values; we would like to use these data to estimate the GP model for the simulator output. The three experiments give an additional 96 values. Hence, a direct application of this univariate formulation is not computationally feasible.

Our experience is that high-dimensional simulation output is the rule, rather than the exception. Hence, a rather general solution to this problem is of considerable value. One approach is to exploit the kronecker structure in the simulation output as in Williams et al. (2006). However

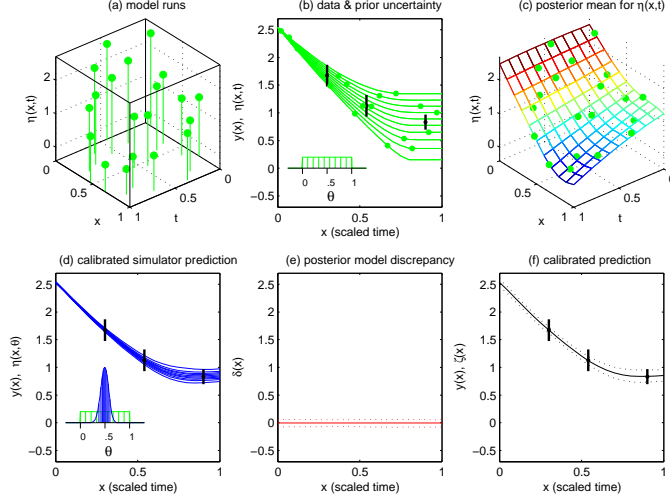


Figure 5: Univariate model formulation applied to a simplified implosion application. (a) An initial set of simulation runs are carried out over the input settings  $(x_j^*, t_j^*), j = 1, \dots, m$ . (b) Experimental data are collected at  $n = 3$  input settings; data are given by the black dots; 90% uncertainties are given by the black lines. The green circles correspond to the  $m = 20$  simulation output values. (c) Posterior mean estimate for the simulator output  $\eta(x, t)$ . (d) Posterior distribution for the calibration parameter  $\theta$  and the resulting simulator-based predictions (blue lines). (e) Posterior mean estimate and pointwise 90% prediction intervals for the model discrepancy term  $\delta(x)$ . (f) Posterior mean estimate and pointwise 90% prediction intervals for the implosion, giving radius as a function of time for the physical system  $\zeta(x)$ .

this approach results in a rather inflexible covariance specification for the GP models and requires that the experimental data be iid on the same support as the simulation output. The approach we present here is applicable in a far wider array of applications, including the HE cylinder application of Sec. 3 which has temporal dependence in the experimental error. In the sections below we briefly comment on design of the simulation runs, describe a basis representation for the simulator output, as well as for the discrepancy to deal with the high dimensionality of the problem. These components are combined into a complete model formulation described in Section 2.2.4. We use Neddermeyer’s implosion application as a vehicle to describe this general approach.

### 2.2.1 Design of simulator runs

A sequence of simulation runs is carried out at  $m$  input settings varying over predefined ranges for each of the input variables:

$$\begin{pmatrix} \mathbf{x}_1^* & \mathbf{t}_1^* \\ \vdots & \vdots \\ \mathbf{x}_m^* & \mathbf{t}_m^* \end{pmatrix} = \begin{pmatrix} x_{11}^* & \cdots & x_{1p_x}^* & t_{11}^* & \cdots & t_{1p_t}^* \\ \vdots & \ddots & \vdots & \vdots & \ddots & \vdots \\ x_{m1}^* & \cdots & x_{mp_x}^* & t_{m1}^* & \cdots & t_{mp_t}^* \end{pmatrix}. \quad (4)$$

We would like to use this collection of simulation runs to screen inputs as well as to build simulator predictions at untried input settings using a Gaussian process model.

We typically use space filling Latin hypercube (LH) designs (Tang, 1993; Ye et al., 2000; Leary et al., 2003) to generate simulation runs in the applications we encounter. Such designs spread points evenly in higher dimensional margins, while maintaining the benefits of the LH design.

We standardize the inputs to range over  $[0, 1]^{p_x+p_t}$  to facilitate the design and prior specification (described later). Specifically, for the cylinder application, we use a strength 2, orthogonal array (OA)-based LH design for the simulation runs. The OA design is over  $p_x + p_t = 1 + 2 = 3$  factors, with each factor having four levels equally spaced between 0 and 1:  $\frac{1}{8}, \frac{3}{8}, \frac{5}{8}, \frac{7}{8}$ . We have found that in practice, this design of simulation runs is often built up sequentially.

For the cylinder application, the output from the resulting simulator runs is shown in Figure 6. The simulator gives the radius of the inner shell of the cylinder over a fixed grid of times and angle. Surfaces from the left-hand frame are the output of three different simulations. Due to the

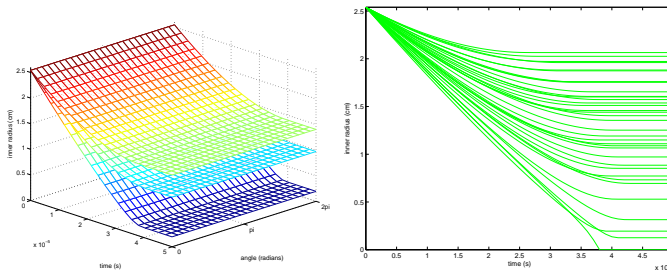


Figure 6: Simulated implusions using input settings from the OA-based LH design. Simulation output gives radius by time ( $\tau$ ) and angle ( $\phi$ ) as shown in the left-hand figure. The radius by time trajectories are shown for all  $m = 36$  simulations in the right-hand figure.

symmetry assumptions in the simulator, the simulated inner radius only changes with time  $\tau$ —not angle  $\phi$ . However, since the experimental data give radius values that vary by angle at fixed sets of times (Figure 3), we treat the simulator output as an image of radii over time  $t$  and angle  $\phi$ . All  $m = 36$  simulations are shown in the right frame of Figure 6 as a function of time only. It is worth noting that the simulations always give the output on this fixed grid over time and angle. This is in contrast to the comparatively irregular collection of experimental data that varies substantially as to its amount as well as which angles and times the radius is measured.

### 2.2.2 Simulator model

Our analysis requires we develop a probability model to describe the simulator output at untried settings  $(\mathbf{x}, \mathbf{t})$ . To do this, we use the simulator outputs to construct a GP model that “emulates” the simulator at arbitrary input settings over the (standardized) design space  $[0, 1]^{p_x+p_t}$ . To construct this emulator, we model the simulation output using a  $p_\eta$ -dimensional basis representation:

$$\boldsymbol{\eta}(\mathbf{x}, \mathbf{t}) = \sum_{i=1}^{p_\eta} \mathbf{k}_i w_i(\mathbf{x}, \mathbf{t}) + \boldsymbol{\epsilon}, (\mathbf{x}, \mathbf{t}) \in [0, 1]^{p_x+p_t}, \quad (5)$$

where  $\{\mathbf{k}_1, \dots, \mathbf{k}_{p_\eta}\}$  is a collection of orthogonal,  $n_\eta$ -dimensional basis vectors, the  $w_i(\mathbf{x}, \mathbf{t})$ 's are GPs over the input space, and  $\boldsymbol{\epsilon}$  is a  $n_\eta$ -dimensional error term. This type of formulation reduces the problem of building an emulator that maps  $[0, 1]^{p_x+p_t}$  to  $R^{n_\eta}$  to building  $p_\eta$  independent, univariate GP models for each  $w_i(\mathbf{x}, \mathbf{t})$ . The details of this model specification are given below.

The simulations rarely give incomplete output, so this output can often be efficiently represented via principal components (Ramsay and Silverman, 1997). After subtracting out the mean simulation and possibly scaling the simulation output, we collect the  $m$  simulations in vectors of length  $n_\eta$ .

These standardized simulations are stored in the  $n_\eta \times m$  matrix  $\Xi$ . We obtain the basis vectors  $\mathbf{K}_\eta = [\mathbf{k}_1; \dots; \mathbf{k}_{p_\eta}]$  via singular value decomposition (SVD) of the standardized simulation output matrix  $\Xi$ . We also scale each  $\mathbf{k}_i$  so that each  $w_i(\mathbf{x}, \mathbf{t})$  process can be modeled with a mean of 0 and a marginal variance close to 1.

Our choice for the number of basis vectors is currently ad-hoc. We would like to accurately model the simulator output. This leads us to select  $p_\eta$  so that at least 99% of the variance in the  $m$  simulations is explained. Our experience is that this takes no more than 5 PC bases for the types of physical systems we typically work with. We have also found that the GP model  $w_i(\mathbf{x}, \mathbf{t})$  predicts well for the first few components, but eventually predicts poorly for the latter components. These latter components typically explain no more than .05% of the variation and do not add to the predictive ability of the GP model. Hence we determine  $p_\eta$  on a case by case basis with these issues in mind.

For the cylinder example we take  $p_\eta = 3$  so that  $\mathbf{K}_\eta = [\mathbf{k}_1; \mathbf{k}_2; \mathbf{k}_3]$ ; the basis functions  $\mathbf{k}_1$ ,  $\mathbf{k}_2$  and  $\mathbf{k}_3$  are shown in Figure 7. Note that the  $\mathbf{k}_i$ 's do not change with angle  $\phi$  due to the angular invariance of Neddermeyer's simulation model.

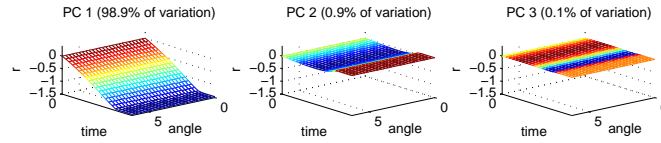


Figure 7: Principal component bases derived from the simulation output.

We use the basis representation of (5) to model the  $n_\eta$ -dimensional simulator output over the input space. Each PC weight  $w_i(\mathbf{x}, \mathbf{t})$ ,  $i = 1, \dots, p_\eta$ , is then modeled as a mean 0 GP

$$w_i(\mathbf{x}, \mathbf{t}) \sim \text{GP}(0, \lambda_{wi}^{-1} R((\mathbf{x}, \mathbf{t}), (\mathbf{x}', \mathbf{t}'); \boldsymbol{\rho}_{wi})),$$

where the covariance function is given by (1) with marginal precision  $\lambda_{wi}$  and correlation distances for each input dimension given by the  $(p_x + p_t)$ -vector  $\boldsymbol{\rho}_{wi}$ .

We define the  $m$ -vector  $\mathbf{w}_i$  to be the restriction of the process  $w_i(\cdot, \cdot)$  to the input design settings given in (4),  $\mathbf{w}_i = (w_i(\mathbf{x}_1^*, \mathbf{t}_1^*), \dots, w_i(\mathbf{x}_m^*, \mathbf{t}_m^*))^T$ ,  $i = 1, \dots, p_\eta$ . In addition we define  $\mathbf{R}((\mathbf{x}^*, \mathbf{t}^*); \boldsymbol{\rho}_{wi})$  to be the  $m \times m$  correlation matrix resulting from applying (1) using  $\boldsymbol{\rho}_{wi}$  to each pair of input settings in the design. The  $mp_\eta$ -vector  $\mathbf{w} = (\mathbf{w}_1^T, \dots, \mathbf{w}_{p_\eta}^T)^T$  has prior distribution

$$\mathbf{w} \sim N(\mathbf{0}_{mp_\eta}, \text{diag}(\lambda_{wi}^{-1} \mathbf{R}((\mathbf{x}^*, \mathbf{t}^*); \boldsymbol{\rho}_{wi}); i = 1, \dots, p_\eta)), \quad (6)$$

which is controlled by  $p_\eta$  precision parameters held in  $\boldsymbol{\lambda}_w$  and  $p_\eta(p_x + p_t)$  spatial correlation parameters held in  $\boldsymbol{\rho}_w$ . The centering of the simulation output makes the zero mean prior appropriate. The prior above can be written more compactly as  $\mathbf{w} \sim N(\mathbf{0}_{mp_\eta}, \boldsymbol{\Sigma}_w)$ , where  $\boldsymbol{\Sigma}_w$  is given in (6).

We specify independent  $\Gamma(a_w, b_w)$  priors for each  $\lambda_{wi}$  and independent  $\text{Beta}(a_{\rho_w}, b_{\rho_w})$  priors for the  $\rho_{wik}$ 's.

$$\begin{aligned} \pi(\lambda_{wi}) &\propto \lambda_{wi}^{a_w-1} e^{-b_w \lambda_{wi}}, \quad i = 1, \dots, p_\eta, \\ \pi(\rho_{wik}) &\propto \rho_{wik}^{a_{\rho_w}-1} (1 - \rho_{wik})^{b_{\rho_w}-1}, \quad i = 1, \dots, p_\eta, \quad k = 1, \dots, p_x + p_t. \end{aligned}$$

We expect the marginal variance for each  $w_i(\cdot, \cdot)$  process to be close to one due to the standardization of the simulator output. For this reason we specify that  $a_w = b_w = 5$ . In addition, this informative

prior helps stabilize the resulting posterior distribution for the correlation parameters which can trade off with the marginal precision parameter (Kern, 2000).

Because we expect only a subset of the inputs to influence the simulator response, our prior for the correlation parameters reflects this expectation of “effect sparsity.” Under the parameterization in (1), input  $k$  is inactive for PC  $i$  if  $\rho_{wik} = 1$ . Choosing  $a_{\rho_w} = 1$  and  $0 < b_{\rho_w} < 1$  will give a density with substantial prior mass near 1. For the cylinder example we take  $b_{\rho_w} = 0.1$ , which makes  $\Pr(\rho_{wik} < 0.98) \approx \frac{1}{3}$  a priori. In general, the selection of these hyperparameters should depend on how many of the  $p_x + p_t$  inputs are expected to be active. An alternative prior for each element of  $\boldsymbol{\rho}_w$  has a point mass at 1, and spreads the rest of the prior probability between 0 and 1. We have found both priors lead to very similar posterior predictions (Linkletter et al., 2006). Although  $p_x + p_t$  is small for this particular application, analyses of modern implosion experiments have involved as many as 60 different inputs.

If we take the error vector in the basis representation of (5) to be i.i.d. normal, we can then develop the sampling model for the simulator output. We define the  $mn_\eta$ -vector  $\boldsymbol{\eta}$  to be the concatenation of all  $m$  simulation output vectors  $\boldsymbol{\eta} = \text{vec}(\boldsymbol{\Xi})$ . Given precision  $\lambda_\eta$  of the errors, the sampling model is then

$$\boldsymbol{\eta} \sim N(\mathbf{0}_{mn_\eta}, \mathbf{K}\boldsymbol{\Sigma}_w\mathbf{K}^T + \lambda_\eta^{-1}\mathbf{I}_{mn_\eta}),$$

where the  $mn_\eta \times mp_\eta$  matrix  $\mathbf{K}$  is given by  $\mathbf{K} = [\mathbf{I}_m \otimes \mathbf{k}_1; \dots; \mathbf{I}_m \otimes \mathbf{k}_{p_\eta}]$ , and the  $\mathbf{k}_i$ ’s are the  $p_\eta$  basis vectors previously computed via SVD. A  $\Gamma(a_\eta, b_\eta)$  prior is specified for the error precision  $\lambda_\eta$ .

### 2.2.3 Discrepancy model

The model for the simulator response is one component of the complete model formulation, which uses experimental data to calibrate the parameter vector  $\mathbf{t}$  as well as account for inadequacies in the simulator. We closely follow the formulation of Kennedy and O’Hagan (2001). Here a vector of experimental observations  $\mathbf{y}(\mathbf{x})$  taken at input condition  $\mathbf{x}$  is modeled as

$$\mathbf{y}(\mathbf{x}) = \boldsymbol{\eta}(\mathbf{x}, \boldsymbol{\theta}) + \boldsymbol{\delta}(\mathbf{x}) + \mathbf{e},$$

where  $\boldsymbol{\eta}(\mathbf{x}, \boldsymbol{\theta})$  is the simulated output at the true parameter setting  $\boldsymbol{\theta}$ ,  $\boldsymbol{\delta}(\mathbf{x})$  accounts for discrepancy between the simulator and physical reality, and  $\mathbf{e}$  models observation error. For discussion and motivation regarding this particular decomposition see Kennedy and O’Hagan (2001) and accompanying discussion.

Previously, Section 2.2.2 gave a detailed explanation of our GP model for  $\boldsymbol{\eta}(\mathbf{x}, \mathbf{t})$ . In this section we define the discrepancy model which, like the model for  $\boldsymbol{\eta}(\mathbf{x}, \mathbf{t})$ , is constructed using a basis representation, placing GP models on the basis weights. It differs in that the basis weights depend only on input condition  $\mathbf{x}$  and that the basis specification for  $\boldsymbol{\delta}(\mathbf{x})$  is typically nonorthogonal and tailored to the application at hand.

For this example consisting of imploding steel cylinders,  $\boldsymbol{\delta}(\mathbf{x})$  adjusts the simulated radius over the time  $\times$  angle grid. This discrepancy between actual and simulated radius is constructed as a linear combination of  $p_\delta = 24$  basis functions that are referenced by the  $n_\eta = 20 \times 26$  grid over time  $\tau$  and angle  $\phi$ . Thus

$$\boldsymbol{\delta}(\mathbf{x}) = \sum_{k=1}^{p_\delta} \mathbf{d}_k(\tau, \phi) v_k(\mathbf{x}) = \sum_{k=1}^{p_\delta} \mathbf{d}_k v_k(\mathbf{x}), \quad (7)$$

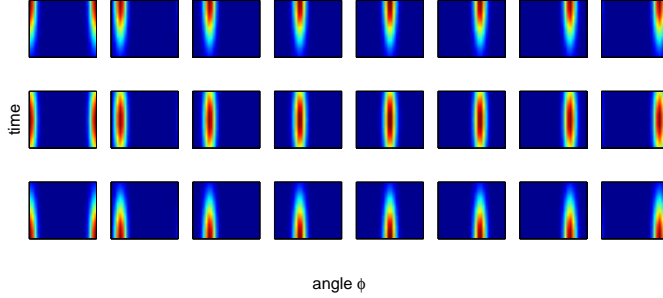


Figure 8: Basis kernels  $\mathbf{d}_k$ ,  $k = 1, \dots, p_\delta$ . Each kernel is a  $n_\eta = 20 \times 26$  image over time ( $y$ -axis) and angle ( $x$ -axis). Note that the basis elements are periodic over angle  $\phi$ .

where the basis functions  $\mathbf{d}_k$ ,  $k = 1, \dots, p_\delta$ , are shown in Figure 8, and independent GP priors over  $\mathbf{x}$  are specified for each weight  $v_k(\mathbf{x})$ .

The basis functions are specified according to what is known about the actual physical process and potential deficiencies in the simulator. Here the basis functions are separable normal kernels that are long in the  $\tau$  direction and narrow and periodic in the  $\phi$  direction. This conforms to our expectation that discrepancies—if they exist—should have a strong time persistence, with a much weaker angular persistence. Given our choice of basis kernel here, the number of bases  $p_\delta$  required depends on the kernel width in the time and angle directions. A spacing between kernels of about one standard deviation in the component directions is required to result in a satisfactory model for  $\delta(\mathbf{x})$  (Higdon, 1998).

The discrepancy basis vectors are divided into  $F$  groups  $G_1, \dots, G_F$ , with the basis coefficients in each group,  $\mathbf{v}_i(\mathbf{x}) = (v_{i,1}(\mathbf{x}), \dots, v_{i,|G_i|}(\mathbf{x}))^T$ , modeled as independent mean 0 GP priors

$$\mathbf{v}_i(\mathbf{x}) \sim GP(\mathbf{0}_{|G_i|}, \lambda_{vi}^{-1} \mathbf{I}_{|G_i|} \otimes R((\mathbf{x}, \mathbf{x}'); \boldsymbol{\rho}_{vi})), \quad i = 1, \dots, F,$$

where  $\lambda_{vi}$  is the common marginal precision of each element in  $\mathbf{v}_i(\mathbf{x})$ ,  $\boldsymbol{\rho}_{vi}$  is a  $p_x$ -vector controlling the correlation strength along each component of  $\mathbf{x}$ , and  $R((\mathbf{x}, \mathbf{x}'); \boldsymbol{\rho}_{vi})$  is the stationary Gaussian product correlation model of (2). The  $F$  precision parameters are held in  $\boldsymbol{\lambda}_v$  and  $Fp_x$  spatial correlation parameters are held in  $\boldsymbol{\rho}_v$ . The Gaussian form of the correlation will enforce a high degree of smoothness for each process  $v_{i,j}(\mathbf{x})$  as a function of  $\mathbf{x}$ . We feel this is plausible in the cylinder application since we expect any discrepancies to change smoothly with input condition  $\mathbf{x}$ . Other applications may require an alternate specification. Often, as in this example, it is sufficient to have common precision and correlation distance parameters for all basis coefficients, i.e.  $F = 1$  and  $p_\delta = |G_1|$ .

As with the GP model for the simulator  $\eta(\mathbf{x}, \mathbf{t})$ , we complete the discrepancy model formulation by specifying gamma priors for the precisions  $\lambda_{vi}$  and independent beta priors for the components of  $\boldsymbol{\rho}_{vi}$ ,

$$\begin{aligned} \pi(\lambda_{vi}) &\propto \lambda_{vi}^{a_v-1} e^{-b_v \lambda_{vi}} \\ \pi(\rho_{vik}) &\propto \rho_{vik}^{a_{\rho_v}-1} (1 - \rho_{vik})^{b_{\rho_v}-1}, \quad i = 1, \dots, F, \quad k = 1, \dots, p_x. \end{aligned}$$

In this application,  $a_v = 1$ ,  $b_v = 0.0001$ ,  $a_{\rho_v} = 1$ , and  $b_{\rho_v} = 0.1$ . This results in a rather uninformative prior for the precision  $\lambda_{v1}$ . If the data are uninformative about this parameter, it will tend to stay at large values that are consistent with a very small discrepancy. Like the prior for  $\boldsymbol{\rho}_w$ , we take  $a_{\rho_v} = 1$  and  $b_{\rho_v} = 0.1$  to encourage effect sparsity.

### 2.2.4 Complete formulation

Given the model specifications for the simulator  $\boldsymbol{\eta}(\mathbf{x}, \mathbf{t})$  and the discrepancy  $\boldsymbol{\delta}(\mathbf{x})$ , we can now consider the sampling model for the experimentally observed data. We assume the data  $\mathbf{y}(\mathbf{x}_1), \dots, \mathbf{y}(\mathbf{x}_n)$  are collected for  $n$  experiments at input conditions  $\mathbf{x}_1, \dots, \mathbf{x}_n$ . For the implosion example, there are  $n = 3$  experiments whose data are shown in Figure 3. Each  $\mathbf{y}(\mathbf{x}_i)$  is a collection of  $n_{y_i}$  measurements over points indexed by time and angle configurations  $(\tau_{i1}, \phi_{i1}), \dots, (\tau_{in_{y_i}}, \phi_{in_{y_i}})$ . The data for experiment  $i$  is modeled as the sum of the simulator output at the true, but unknown, parameter setting  $\boldsymbol{\theta}$  and the discrepancy

$$\mathbf{y}(\mathbf{x}_i) = \boldsymbol{\eta}(\mathbf{x}_i, \boldsymbol{\theta}) + \boldsymbol{\delta}(\mathbf{x}_i) + \mathbf{e}_i,$$

where the observation error vector  $\mathbf{e}_i$  is modeled as  $N(\mathbf{0}_{n_{y_i}}, (\lambda_y \mathbf{W}_i)^{-1})$ . Using the basis representations for the simulator and the discrepancies, this becomes

$$\mathbf{y}(\mathbf{x}_i) = \mathbf{K}_i \mathbf{w}(\mathbf{x}_i, \boldsymbol{\theta}) + \mathbf{D}_i \mathbf{v}(\mathbf{x}_i) + \mathbf{e}_i.$$

Because the time  $\times$  angle support of each  $\mathbf{y}(\mathbf{x}_i)$  varies with experiment and is not necessarily contained in the support of the simulation output, the basis vectors in  $\mathbf{K}_i$  may have to be interpolated over time and angle from  $\mathbf{K}_\eta$ . Since the simulation output over time and angle is quite dense, this interpolation is straightforward. The discrepancy basis matrix  $\mathbf{D}_i$  is determined by the functional form given in (7)—the  $jk$  element of  $\mathbf{D}_i$  is given by  $\mathbf{D}_{i,jk} = \mathbf{d}_k(\tau_{ij}, \phi_{ij})$ .

Taking all of the experiments together, the sampling model is  $n_y$ -variate normal, where  $n_y = n_{y_1} + \dots + n_{y_n}$  is the total number of experimental data points. We define  $\mathbf{y}(\mathbf{e})$  to be the  $n_y$ -vector from concatenation of the  $\mathbf{y}(\mathbf{x}_i)$ 's ( $\mathbf{e}_i$ 's),  $\mathbf{v} = \text{vec}([\mathbf{v}(\mathbf{x}_1); \dots; \mathbf{v}(\mathbf{x}_n)]^T)$  and  $\mathbf{u}(\boldsymbol{\theta}) = \text{vec}([\mathbf{w}(\mathbf{x}_1, \boldsymbol{\theta}); \dots; \mathbf{w}(\mathbf{x}_n, \boldsymbol{\theta})]^T)$ . The sampling model for the entire experimental dataset can be written as

$$\mathbf{y} \sim N(\mathbf{0}_{n_y}, \mathbf{B} \text{diag}(\boldsymbol{\Sigma}_v, \boldsymbol{\Sigma}_u) \mathbf{B}^T + (\lambda_y \mathbf{W}_y)^{-1}),$$

where  $\mathbf{W}_y = \text{diag}(\mathbf{W}_1, \dots, \mathbf{W}_n)$ ,  $\mathbf{B} = [\text{diag}(\mathbf{D}_1, \dots, \mathbf{D}_n); \text{diag}(\mathbf{K}_1, \dots, \mathbf{K}_n)] \text{diag}(\mathbf{P}_D^T, \mathbf{P}_K^T)$ , and  $\mathbf{P}_D$  and  $\mathbf{P}_K$  are permutation matrices whose rows are given by  $\mathbf{P}_D(j + n(i-1); \cdot) = \mathbf{e}_{(j-1)p_\delta + i}^T$ ,  $i = 1, \dots, p_\delta; j = 1, \dots, n$  and  $\mathbf{P}_K(j + n(i-1); \cdot) = \mathbf{e}_{(j-1)p_\eta + i}^T$ ,  $i = 1, \dots, p_\eta; j = 1, \dots, n$ . Note that permutations are required for specifying  $\mathbf{B}$  since the basis weight components have been separated in the definitions of  $\mathbf{v}$  and  $\mathbf{u}(\boldsymbol{\theta})$ . The covariance matrix  $\boldsymbol{\Sigma}_v = \text{diag}(\lambda_{v_i}^{-1} \mathbf{I}_{|G_i|} \otimes \mathbf{R}(\mathbf{x}; \boldsymbol{\rho}_{v_i}); i = 1, \dots, F)$  where  $\mathbf{R}(\mathbf{x}; \boldsymbol{\rho}_{v_i})$  is the  $n \times n$  correlation matrix resulting from applying (2) to each pair of experimental input settings, and  $\boldsymbol{\Sigma}_u = \text{diag}(\lambda_{w_i}^{-1} \mathbf{R}(\mathbf{x}, \boldsymbol{\theta}; \boldsymbol{\rho}_{w_i}); i = 1, \dots, p_\eta)$  where  $\mathbf{R}(\mathbf{x}, \boldsymbol{\theta}; \boldsymbol{\rho}_{w_i})$  is the  $n \times n$  correlation matrix resulting from applying (1) to each pair of experimental input settings (correlations depend only on the  $\mathbf{x}$ -dimensions as  $\mathbf{t} = \boldsymbol{\theta}$  is common to all elements of  $\mathbf{u}(\boldsymbol{\theta})$ ). A  $\Gamma(a_y, b_y)$  prior is specified for the observational error precision  $\lambda_y$ . The observation precision  $\mathbf{W}_y$  is often fairly well-known in practice. Hence we use an informative prior for  $\lambda_y$  that encourages its value to be near one. In the implosion example we set  $a_y = b_y = 5$ .

It is now possible to specify the joint sampling model of the observables  $\mathbf{y}$  and  $\boldsymbol{\eta}$ . The  $(n(p_\delta + p_\eta) + mp_\eta)$ -vector  $\mathbf{z} = (\mathbf{v}^T, \mathbf{u}^T(\boldsymbol{\theta}), \mathbf{w}^T)^T$  has prior distribution

$$\mathbf{z} \sim N \left( \mathbf{0}_{n(p_\delta + p_\eta) + mp_\eta}, \boldsymbol{\Sigma}_z = \begin{pmatrix} \boldsymbol{\Sigma}_v & \mathbf{0} & \mathbf{0} \\ \mathbf{0} & \boldsymbol{\Sigma}_u & \boldsymbol{\Sigma}_{u,w} \\ \mathbf{0} & \boldsymbol{\Sigma}_{u,w}^T & \boldsymbol{\Sigma}_w \end{pmatrix} \right),$$

where  $\Sigma_v$ ,  $\Sigma_u$  and  $\Sigma_w$  have been defined previously, and  $\Sigma_{u,w} = \text{diag}(\lambda_{wi}^{-1} \mathbf{R}((\mathbf{x}, \boldsymbol{\theta}), (\mathbf{x}^*, \mathbf{t}^*); \boldsymbol{\rho}_{wi}); i = 1, \dots, p_\eta)$  where  $\mathbf{R}((\mathbf{x}, \boldsymbol{\theta}), (\mathbf{x}^*, \mathbf{t}^*); \boldsymbol{\rho}_{wi})$  denotes the  $n \times m$  cross-correlation matrix for the GP modeling the simulator output obtained by applying (1) to the  $n$  experimental settings  $(\mathbf{x}_1, \boldsymbol{\theta}), \dots, (\mathbf{x}_n, \boldsymbol{\theta})$  crossed with the  $m$  simulator input settings  $(\mathbf{x}_1^*, \mathbf{t}_1^*), \dots, (\mathbf{x}_m^*, \mathbf{t}_m^*)$ . Since

$$\begin{pmatrix} \mathbf{y} \\ \boldsymbol{\eta} \end{pmatrix} = \begin{pmatrix} \mathbf{B} & \mathbf{0} \\ \mathbf{0} & \mathbf{K} \end{pmatrix} \mathbf{z} + \begin{pmatrix} \mathbf{e} \\ \boldsymbol{\epsilon} \end{pmatrix}, \quad (8)$$

and the error terms are multivariate normal, the joint sampling distribution of  $\mathbf{y}$  and  $\boldsymbol{\eta}$  is also multivariate normal.

Compiling the developments beginning in Section 2.2.2, the posterior distribution of the calibration and statistical model parameters has the form

$$\begin{aligned} \pi(\lambda_\eta, \boldsymbol{\lambda}_w, \boldsymbol{\rho}_w, \lambda_y, \boldsymbol{\lambda}_v, \boldsymbol{\rho}_v, \boldsymbol{\theta} | \mathbf{y}, \boldsymbol{\eta}) &\propto \quad (9) \\ L(\mathbf{y}, \boldsymbol{\eta} | \lambda_\eta, \boldsymbol{\lambda}_w, \boldsymbol{\rho}_w, \lambda_y, \boldsymbol{\lambda}_v, \boldsymbol{\rho}_v, \boldsymbol{\theta}) &\times \lambda_\eta^{a_\eta - 1} e^{-b_\eta \lambda_\eta} \times \prod_{i=1}^{p_\eta} \lambda_{wi}^{a_w - 1} e^{-b_w \lambda_{wi}} \times \\ \prod_{i=1}^{p_\eta} \prod_{k=1}^{p_x + p_t} \rho_{wik}^{a_{\rho_w} - 1} (1 - \rho_{wik})^{b_{\rho_w} - 1} &\times \lambda_y^{a_y - 1} e^{-b_y \lambda_y} \times \prod_{i=1}^F \lambda_{vi}^{a_v - 1} e^{-b_v \lambda_{vi}} \times \\ \prod_{i=1}^F \prod_{k=1}^{p_x} \rho_{vik}^{a_{\rho_v} - 1} (1 - \rho_{vik})^{b_{\rho_v} - 1} &\times I[\boldsymbol{\theta} \in C], \end{aligned}$$

where  $L(\mathbf{y}, \boldsymbol{\eta} | \cdot)$  denotes the multivariate normal sampling distribution of  $\mathbf{y}$  and  $\boldsymbol{\eta}$ , and  $C$  denotes the constraint region for  $\boldsymbol{\theta}$ , which is typically a  $p_t$ -dimensional rectangle. In other applications  $C$  can also incorporate constraints among the components of  $\boldsymbol{\theta}$ .

Computation of  $L(\mathbf{y}, \boldsymbol{\eta} | \cdot)$  is cumbersome given the large amount of functional experimental data and simulator output typically available for analysis. The following result can be used to substantially reduce the burden of this computation:

**Result 1.** Suppose  $\boldsymbol{\beta} \sim N(\mathbf{0}, \Sigma_\beta)$  and  $\boldsymbol{\varepsilon} \sim N(\mathbf{0}, \Sigma_\varepsilon)$ . Let  $\boldsymbol{\omega} = \mathbf{C}\boldsymbol{\beta} + \boldsymbol{\varepsilon}$  where  $\mathbf{C}$  has full column rank. Then

$$L(\boldsymbol{\omega}) \propto |\Sigma_\varepsilon|^{-1/2} |\mathbf{C}^T \Sigma_\varepsilon^{-1} \mathbf{C}|^{-1/2} \exp \left[ -\frac{1}{2} \boldsymbol{\omega}^T \left( \Sigma_\varepsilon^{-1} - \Sigma_\varepsilon^{-1} \mathbf{C} (\mathbf{C}^T \Sigma_\varepsilon^{-1} \mathbf{C})^{-1} \mathbf{C}^T \Sigma_\varepsilon^{-1} \right) \boldsymbol{\omega} \right] L(\hat{\boldsymbol{\beta}}),$$

where  $\hat{\boldsymbol{\beta}} = (\mathbf{C}^T \Sigma_\varepsilon^{-1} \mathbf{C})^{-1} \mathbf{C}^T \Sigma_\varepsilon^{-1} \boldsymbol{\omega}$ .

This result holds in slightly altered form if  $\mathbf{C}$  is not of full column rank: set  $\mathbf{C} = \tilde{\mathbf{C}}\mathbf{L}$  where  $\tilde{\mathbf{C}}$  contains a basis for the column space of  $\mathbf{C}$  and  $\mathbf{L}$  is of full row rank. The result applies to  $\boldsymbol{\omega} = \tilde{\mathbf{C}}\boldsymbol{\beta} + \boldsymbol{\varepsilon}$  for  $\hat{\boldsymbol{\beta}} = \mathbf{L}\boldsymbol{\beta}$  regardless of basis chosen for  $\tilde{\mathbf{C}}$ . Alternatively, if  $\mathbf{C}$  is not of full column rank,  $\mathbf{C}^T \Sigma_\varepsilon^{-1} \mathbf{C}$  may be replaced by  $\mathbf{C}^T \Sigma_\varepsilon^{-1} \mathbf{C} + r\mathbf{I}$  where  $r$  is a small ridge.

Applying Result 1 to (8), we obtain

$$\begin{aligned} L(\mathbf{y}, \boldsymbol{\eta} | \cdot) &\propto \lambda_\eta^{m(n_\eta - p_\eta)/2} \exp \left[ -\frac{1}{2} \lambda_\eta \boldsymbol{\eta}^T \left( \mathbf{I} - \mathbf{K} (\mathbf{K}^T \mathbf{K})^{-1} \mathbf{K}^T \right) \boldsymbol{\eta} \right] \times \quad (10) \\ \lambda_y^{(n_y - \text{rank}(\mathbf{B})) / 2} &\exp \left[ -\frac{1}{2} \lambda_y \mathbf{y}^T \left( \mathbf{W}_y - \mathbf{W}_y \mathbf{B} (\mathbf{B}^T \mathbf{W}_y \mathbf{B})^{-1} \mathbf{B}^T \mathbf{W}_y \right) \mathbf{y} \right] \times L(\hat{\mathbf{z}} | \cdot), \end{aligned}$$

where  $\hat{\mathbf{z}} = \text{vec}([(B^T W_y B)^{-1} B^T W_y \mathbf{y}; (K^T K)^{-1} K^T \boldsymbol{\eta}])$  and  $L(\hat{\mathbf{z}}|\cdot)$  is computed from

$$\hat{\mathbf{z}} \sim N \left( \mathbf{0}, \boldsymbol{\Sigma}_{\hat{\mathbf{z}}} = \boldsymbol{\Sigma}_z + \begin{pmatrix} (\lambda_y B^T W_y B)^{-1} & \mathbf{0} \\ \mathbf{0} & (\lambda_\eta K^T K)^{-1} \end{pmatrix} \right).$$

The possibility that  $\mathbf{B}$  may not be full rank in some applications is accounted for in (10); in this event, the matrix inverses are handled by reduction to full rank or by including a ridge as described above. Incorporation of these results in (9) gives an equivalent expression for the full posterior distribution

$$\begin{aligned} \pi(\lambda_\eta, \boldsymbol{\lambda}_w, \boldsymbol{\rho}_w, \lambda_y, \boldsymbol{\lambda}_v, \boldsymbol{\rho}_v, \boldsymbol{\theta}|\mathbf{y}, \boldsymbol{\eta}) &\propto & (11) \\ |\boldsymbol{\Sigma}_{\hat{\mathbf{z}}}|^{-1/2} \exp \left[ -\frac{1}{2} \hat{\mathbf{z}}^T \boldsymbol{\Sigma}_{\hat{\mathbf{z}}}^{-1} \hat{\mathbf{z}} \right] &\times \lambda_\eta^{a'_\eta - 1} e^{-b'_\eta \lambda_\eta} \times \prod_{i=1}^{p_\eta} \lambda_{wi}^{a_w - 1} e^{-b_w \lambda_{wi}} \times \\ \prod_{i=1}^{p_\eta} \prod_{k=1}^{p_x + p_t} \rho_{wik}^{a_{\rho_w} - 1} (1 - \rho_{wik})^{b_{\rho_w} - 1} &\times \lambda_y^{a'_y - 1} e^{-b'_y \lambda_y} \times \prod_{i=1}^F \lambda_{vi}^{a_v - 1} e^{-b_v \lambda_{vi}} \times \\ \prod_{i=1}^F \prod_{k=1}^{p_x} \rho_{vik}^{a_{\rho_v} - 1} (1 - \rho_{vik})^{b_{\rho_v} - 1} &\times I[\boldsymbol{\theta} \in C], \end{aligned}$$

where

$$\begin{aligned} a'_\eta &= a_\eta + \frac{m(n_\eta - p_\eta)}{2}; & b'_\eta &= b_\eta + \frac{1}{2} \boldsymbol{\eta}^T \left( \mathbf{I} - \mathbf{K} (\mathbf{K}^T \mathbf{K})^{-1} \mathbf{K}^T \right) \boldsymbol{\eta} \\ a'_y &= a_y + \frac{n_y - \text{rank}(\mathbf{B})}{2}; & b'_y &= b_y + \frac{1}{2} \mathbf{y}^T \left( \mathbf{W}_y - \mathbf{W}_y \mathbf{B} (\mathbf{B}^T \mathbf{W}_y \mathbf{B})^{-1} \mathbf{B}^T \mathbf{W}_y \right) \mathbf{y}. \end{aligned}$$

The required matrix inversion is reduced to order  $n(p_\delta + p_\eta) + mp_\eta$  in (11) from order  $(n_y + mn_\eta)$  in (9)—particularly efficient when  $n_\eta$  and  $n_y$  are large.

Realizations from the posterior distribution are produced using standard, single site MCMC. Metropolis updates (Metropolis et al., 1953) are used for the components of  $\boldsymbol{\rho}_w$ ,  $\boldsymbol{\rho}_v$  and  $\boldsymbol{\theta}$  with a uniform proposal distribution centered at the current value of the parameter. The precision parameters  $\lambda_\eta$ ,  $\boldsymbol{\lambda}_w$ ,  $\lambda_y$  and  $\boldsymbol{\lambda}_v$  are sampled using Hastings (1970) updates. Here the proposals are uniform draws, centered at the current parameter values, with a width that is proportional to the current parameter value. Note that we bound the proposal width by not letting it get below 0.5.

In a given application the candidate proposal width can be tuned for optimal performance. However, because of the way the data have been standardized, we have found that a width of 0.2 for the Metropolis updates, and a width of 0.3 times the current parameter value (or 0.5, whichever is larger) for the Hastings updates, works quite well over a fairly wide range of applications. This has been an important consideration in the development of general software to carry out such analyses.

The resulting posterior distribution estimate for  $(\theta_1, \theta_2)$  in the cylinder application is shown in Figure 9 on the standardized  $C = [0, 1]^2$  scale. This covers the true values of  $\boldsymbol{\theta} = (0.5, 0.5)$  from which the synthetic data were generated.

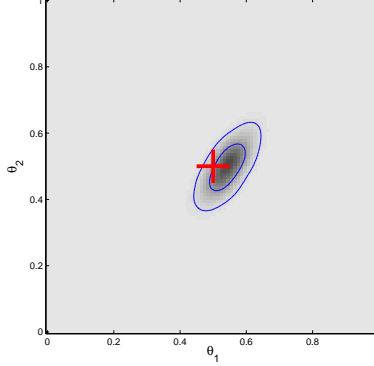


Figure 9: Estimated posterior distribution of the calibration parameters  $(\theta_1, \theta_2)$ , which correspond to the detonation energy of the explosive and the yield stress of steel respectively. The true values from which the data were generated are  $\theta = (0.5, 0.5)$ .

### 2.2.5 Posterior prediction

Given posterior realizations from (11), predictions of the calibrated simulator  $\boldsymbol{\eta}(\mathbf{x}^*, \boldsymbol{\theta})$  and discrepancy term  $\boldsymbol{\delta}(\mathbf{x}^*)$  can be generated at any input setting  $\mathbf{x}^*$ . Predictions of system behavior  $\boldsymbol{\zeta}(\mathbf{x}^*) = \boldsymbol{\eta}(\mathbf{x}^*, \boldsymbol{\theta}) + \boldsymbol{\delta}(\mathbf{x}^*)$  follow. Since  $\boldsymbol{\eta}(\mathbf{x}^*, \boldsymbol{\theta}) = \mathbf{K}\mathbf{w}(\mathbf{x}^*, \boldsymbol{\theta})$  and  $\boldsymbol{\delta}(\mathbf{x}^*) = \mathbf{D}\mathbf{v}(\mathbf{x}^*)$ , we need only produce draws  $\mathbf{w}(\mathbf{x}^*, \boldsymbol{\theta})$  and  $\mathbf{v}(\mathbf{x}^*)$  given a posterior draw of the parameter vector  $(\lambda_\eta, \boldsymbol{\lambda}_w, \boldsymbol{\rho}_w, \lambda_y, \boldsymbol{\lambda}_v, \boldsymbol{\rho}_v, \boldsymbol{\theta})$ . The following result provides a roadmap for generating the necessary realizations:

**Result 2.** Suppose  $\boldsymbol{\beta} \sim N(\mathbf{0}, \boldsymbol{\Sigma}_\beta)$  and  $\boldsymbol{\varepsilon} \sim N(\mathbf{0}, \boldsymbol{\Sigma}_\varepsilon)$ . Let  $\boldsymbol{\omega} = \mathbf{C}\boldsymbol{\beta} + \boldsymbol{\varepsilon}$  where  $\mathbf{C}$  has full column rank. Assume that

$$\begin{pmatrix} \boldsymbol{\beta} \\ \mathbf{b}^* \end{pmatrix} \sim N \left( \begin{pmatrix} \mathbf{0} \\ \mathbf{0} \end{pmatrix}, \begin{pmatrix} \boldsymbol{\Sigma}_\beta & \boldsymbol{\Sigma}_{\beta, \mathbf{b}^*} \\ \boldsymbol{\Sigma}_{\beta, \mathbf{b}^*}^T & \boldsymbol{\Sigma}_{\mathbf{b}^*} \end{pmatrix} \right).$$

The conditional distributions  $\pi(\mathbf{b}^* | \boldsymbol{\omega})$  and  $\pi(\mathbf{b}^* | \hat{\boldsymbol{\beta}})$  are equivalent, where  $\hat{\boldsymbol{\beta}} = (\mathbf{C}^T \boldsymbol{\Sigma}_\varepsilon^{-1} \mathbf{C})^{-1} \mathbf{C}^T \boldsymbol{\Sigma}_\varepsilon^{-1} \boldsymbol{\omega}$ .

If  $\mathbf{C}$  is not full rank, Result 2 holds with the same modifications discussed subsequent to the statement of Result 1. Result 2 indicates that realizations of basis coefficient vectors can be drawn conditional on the reduced data  $\hat{\mathbf{z}}$  rather than the full data  $\mathbf{y}$  and  $\boldsymbol{\eta}$ , resulting in computational cost savings.

These predictions can be produced from standard GP theory. Conditional on the parameter vector  $(\lambda_\eta, \boldsymbol{\lambda}_w, \boldsymbol{\rho}_w, \lambda_y, \boldsymbol{\lambda}_v, \boldsymbol{\rho}_v, \boldsymbol{\theta})$ , the reduced data  $\hat{\mathbf{z}}$ , along with the predictions  $\mathbf{w}(\mathbf{x}^*, \boldsymbol{\theta})$  and  $\mathbf{v}(\mathbf{x}^*)$ , have the joint distribution

$$\begin{pmatrix} \hat{\mathbf{z}} \\ \mathbf{v}(\mathbf{x}^*) \\ \mathbf{w}(\mathbf{x}^*, \boldsymbol{\theta}) \end{pmatrix} \sim N \left( \begin{pmatrix} \mathbf{0} \\ \mathbf{0} \\ \mathbf{0} \end{pmatrix}, \begin{pmatrix} \boldsymbol{\Sigma}_{\hat{\mathbf{z}}} & & \\ \boldsymbol{\Sigma}_{\mathbf{v}^*, \hat{\mathbf{z}}} & \text{diag}(\lambda_{v_i}^{-1} \mathbf{I}_{|G_i|}; i = 1, \dots, F) & \\ \boldsymbol{\Sigma}_{\mathbf{w}^*, \hat{\mathbf{z}}} & \mathbf{0} & \text{diag}(\lambda_{w_i}^{-1}; i = 1, \dots, p_\eta) \end{pmatrix} \right),$$

where  $\boldsymbol{\Sigma}_{\hat{\mathbf{z}}, \mathbf{v}^*}$  has nonzero elements due to the correlation between  $\mathbf{v}$  and  $\mathbf{v}(\mathbf{x}^*)$ , and  $\boldsymbol{\Sigma}_{\hat{\mathbf{z}}, \mathbf{w}^*}$  has nonzero elements due to the correlation between  $(\mathbf{u}(\boldsymbol{\theta}), \mathbf{w})$  and  $\mathbf{w}(\mathbf{x}^*, \boldsymbol{\theta})$ . The exact construction of the matrices  $\boldsymbol{\Sigma}_{\hat{\mathbf{z}}, \mathbf{v}^*}$  and  $\boldsymbol{\Sigma}_{\hat{\mathbf{z}}, \mathbf{w}^*}$  is analogous to the construction of  $\boldsymbol{\Sigma}_{\mathbf{u}, \mathbf{w}}$  in Section 2.2.4. Generating simultaneous draws of  $\mathbf{v}(\mathbf{x}^*)$  and  $\mathbf{w}(\mathbf{x}^*, \boldsymbol{\theta})$  given  $\hat{\mathbf{z}}$  is then straightforward using conditional normal rules (Santner et al., 2003).

The posterior mean estimates for  $\boldsymbol{\eta}(\mathbf{x}^*, \boldsymbol{\theta})$ ,  $\delta(\mathbf{x}^*)$  and their sum,  $\zeta(\mathbf{x}^*)$ , are shown in Figure 10 for the three input conditions  $\mathbf{x}^*$  corresponding to the amount of HE used in each of the three cylinder experiments. Also shown are the experimental data records from each of the experiments. Note that the discrepancy term picks up a consistent signal across experiments that varies with time and angle, even though the simulator cannot give variation by angle  $\phi$ .

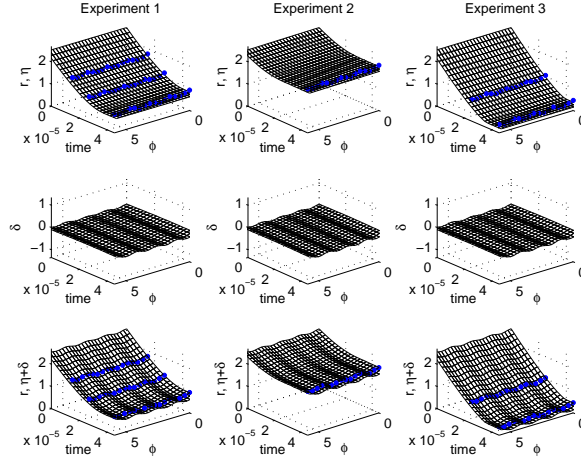


Figure 10: Posterior mean estimates for  $\boldsymbol{\eta}(\mathbf{x}^*, \boldsymbol{\theta})$ ,  $\delta(\mathbf{x}^*)$ , and their sum,  $\zeta(\mathbf{x}^*)$ , at the three input conditions corresponding to each of the three experiments. The experimental observations are given by the dots in the figures showing the posterior means for  $\boldsymbol{\eta}(\mathbf{x}^*, \boldsymbol{\theta})$  and  $\zeta(\mathbf{x}^*)$ .

Figure 11 shows the prediction uncertainty for the inner radius at the photograph times of the three experiments. The figure gives pointwise 90% credible intervals for the inner radius. Here, the prediction for each experiment uses only the data from the other two experiments, making these holdout predictions.

Posterior predictions of the process  $\boldsymbol{\eta}(\cdot, \cdot)$  can be made at any input setting  $(\mathbf{x}^*, \mathbf{t}^*)$ . The GP theory required is analogous to the complete formulation above. Conditional on the parameter vector  $(\lambda_\eta, \boldsymbol{\lambda}_w, \boldsymbol{\rho}_w)$ , the reduced data  $\hat{\mathbf{w}} = (\mathbf{K}^T \mathbf{K})^{-1} \mathbf{K}^T \boldsymbol{\eta}$  and the predictions  $\mathbf{w}(\mathbf{x}^*, \mathbf{t}^*)$  have the joint distribution

$$\begin{pmatrix} \hat{\mathbf{w}} \\ \mathbf{w}(\mathbf{x}^*, \mathbf{t}^*) \end{pmatrix} \sim N \left( \begin{pmatrix} \mathbf{0} \\ \mathbf{0} \end{pmatrix}, \begin{pmatrix} \boldsymbol{\Sigma}_{\hat{\mathbf{w}}} & \boldsymbol{\Sigma}_{\hat{\mathbf{w}}, \mathbf{w}^*} \\ \boldsymbol{\Sigma}_{\mathbf{w}^*, \hat{\mathbf{w}}} & \text{diag}(\lambda_{w_i}^{-1}; i = 1, \dots, p_\eta) \end{pmatrix} \right).$$

Figure 12 shows posterior means for the simulator response  $\boldsymbol{\eta}(\cdot, \cdot)$  of the cylinder application, where each of the three inputs were varied over their prior range of  $[0, 1]$  while the other two inputs were held at their nominal setting of 0.5. The posterior mean response surfaces convey an idea of how the different parameters affect the highly multivariate simulation output. Other marginal functionals of the simulation response can also be calculated such as sensitivity indices or estimates of the Sobol' decomposition (Sacks et al., 1989; Oakley and O'Hagan, 2004).

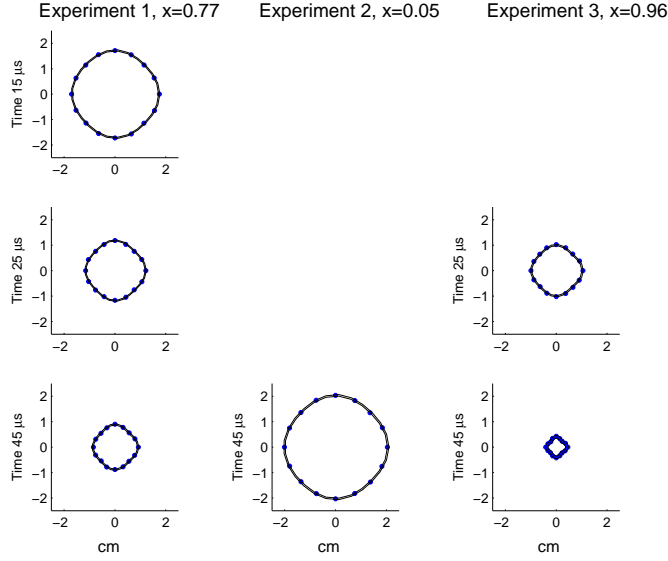


Figure 11: Holdout prediction uncertainty for the inner radius at the photograph times for each experiment. The lines show simultaneous 90% credible intervals; the experimental data is given by the dots.

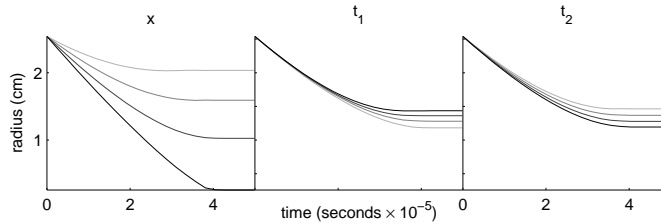


Figure 12: Posterior mean simulator predictions (radius as a function of time) varying 1 input, holding others at their nominal values of 0.5. Darker lines correspond to higher input values.

### 3 Application to HE cylinder experiments

#### 3.1 Experimental setup

Often, analysis of experiments requires that the simulator accurately models a number of different physical phenomena. This is the case with the previous implosion application, which involves imparting energy deposited by an explosive, as well as modeling the deformation of the steel cylinder. The added difficulty of modeling integrated physics effects makes it beneficial to consider additional experiments that better isolate the physical process of interest. The HE cylinder experiment, considered in this section, more cleanly isolates the effects of HE detonation.

The cylinder test has become a standard experiment performed on various types of HE at LANL. The standard version of this experiment—depicted in Figure 13—consists of a thin-walled cylinder of copper surrounding a solid cylinder of the HE of interest. One end of the HE cylinder is initiated with a plane-wave lens; the detonation proceeds down the cylinder of HE, expanding

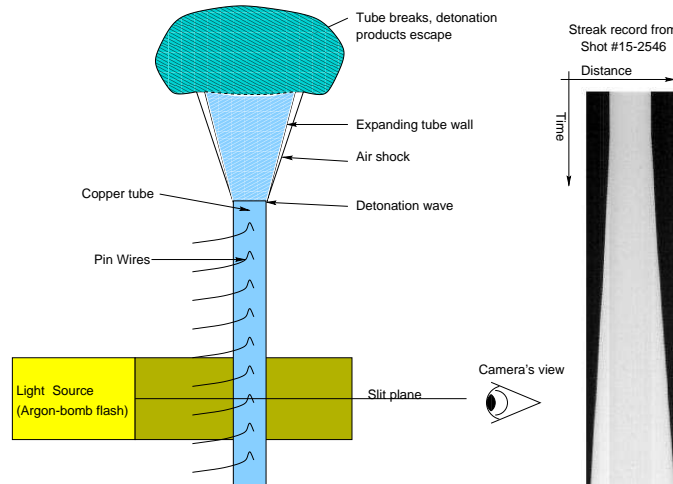


Figure 13: HE cylinder experiment. The HE cylinder is initiated with plane detonation wave, which begins to expand the surrounding copper cylinder as the detonation progresses. This detonation wave moves down the cylinder. Pin wires detect the arrival time of the detonation along the wave, while the streak camera captures the expansion of the detonation wave at a single location on the cylinder.

the copper tube via work done by the rapidly increasing pressure from the HE. As the detonation progresses, the copper cylinder eventually fails.

Diagnostics on this experiment generally include a streak camera to record the expansion of the cylinder, and pin wires at regular intervals along the length of the copper cylinder. Each pin wire shorts as the detonation wave reaches its location, sending a signal that indicates time of arrival of the detonation wave. From these arrival times, the detonation velocity of the experiment can be determined with relatively high accuracy. Note the use of copper in this experiment is necessary to contain the HE as it detonates. Since copper is a well-controlled and understood material, its presence will not greatly affect our ability to simulate the experiment.

Details of the experiments are as follows: HE diameter is 1 inch; copper thickness is 0.1 inch; cylinder length is 30 cm; slit location is 19 cm down from where the cylinder is detonated—by this distance, the detonation wave is essentially in steady state. Prior to the experiment, the initial density of the HE cylinder is measured.

### 3.2 Simulations

Simulations of HE detonation typically involve two major components—the burn, in which the HE rapidly changes phase, from solid to gas, and the equation of state (EOS) for the resulting gas products, which dictates how this gas works on the materials it is pushing against. The detonation velocity, determined by the pin wires, is used to prescribe the burn component of the simulation, moving the planar detonation wave down the cylinder. This empirical approach for modeling the burn accurately captures the detonation for this type of experiment. It is the parameters controlling the EOS of the gaseous HE products that are of interest here.

The EOS describes the state of thermodynamic equilibrium for a fluid (the HE gas products, in this case) at each point in space and time in terms of pressure, internal energy, density, entropy,

and temperature. Thermodynamic considerations allow the EOS to be described by only two of these parameters. In this case, the EOS is determined by a system of equations, giving pressure as a function of density and internal energy.

The HE EOS function is controlled by an 8-dimensional parameter vector  $\mathbf{t}$ . The first component  $t_1$  modifies the energy imparted by the detonation; the second modifies the Gruneisen gamma parameter. The remaining six parameters modify the isentrope lines of the EOS function (pressure-density contours corresponding to constant energy).

Thus we have 9 inputs of interest to the simulation model. The first,  $x_1$ , is the initial density of the HE sample, which is measured prior to the experiment. The remaining  $p_t = 8$  parameters describe the HE EOS. Prior ranges were determined for each of these input settings. They have been standardized so that the nominal setting is 0.5, the minimum is 0, and the maximum is 1. A 128 run OA-based LH design was constructed over this  $p_x + p_t = 9$ -dimensional input space giving the simulation output shown by the gray lines in Figure 14. Of the 128 simulation runs, all but two of them ran to completion. Hence the analysis will be based on the 126 runs that completed.

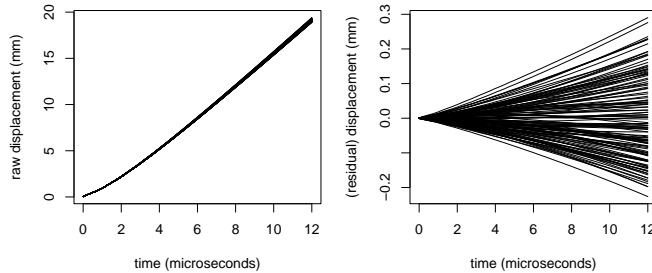


Figure 14: 126 simulated displacement curves for the HE cylinder experiment. Left: simulated displacement of the cylinder where time = 0 corresponds to the arrival of the detonation wave at the camera slit. Right: the residual displacement of the cylinder after subtracting out the pointwise mean of the simulations.

### 3.3 Experimental observations

The top row of Figure 20 shows the experimental data derived from the streak camera from four different HE cylinder experiments. The same adjustment of subtracting out the average simulation is also applied to the data. For comparison, the mean-centered simulations are also given by the gray lines. The cylinder expansion is recorded as time-displacement pairs for both the left- and right-hand sides of the cylinder as seen by the streak record. The measured density (in standardized units) for each of the HE cylinders is 0.15, 0.15, 0.33, 0.56 for Experiments 1–4, respectively.

The data errors primarily come from four different sources: determination of the zero displacement level, causing a random shift in the entire data trace; slight tilting of the cylinder relative to the camera in the experimental setup; replicate variation due to subtle differences in materials used in the various experiments—modeled as time correlated Gaussian errors; and jitter due to the resolution of the film. After substantial discussion with subject matter experts, we decided to model the precision of a given trace  $\ell$ , which indexes side (right or left) as well as experiment as

$$\mathbf{W}_\ell = (\sigma_0^2 \mathbf{1}\mathbf{1}^T + \sigma_t^2 \boldsymbol{\tau}_\ell \boldsymbol{\tau}_\ell^T + \sigma_a^2 \mathbf{R}_\ell + \sigma_j^2 \mathbf{I})^{-1},$$

where  $\mathbf{1}$  denotes the vector of ones and  $\boldsymbol{\tau}_\ell$  denotes the times corresponding to trace  $\ell$ . The variances  $\sigma_0^2$ ,  $\sigma_t^2$ ,  $\sigma_a^2$ , and  $\sigma_j^2$  and correlation matrix  $\mathbf{R}_\ell$  have been elicited from experts. For experiment 3, only a single trace was obtained, resulting in a much larger uncertainty for the tilt in that experiment. Thus the value of  $\sigma_t$  was altered accordingly for that experiment. Note that the model allows for a parameter  $\lambda_y$  to scale the complete data precision matrix  $\mathbf{W}_y$ . Because of the ringing effects in the displacement observations at early times, we take only the data between  $2.5\mu\text{s}$  and  $12.0\mu\text{s}$ .

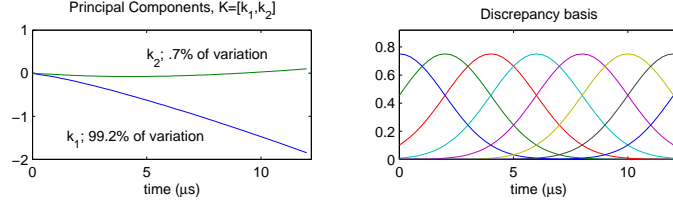


Figure 15: Principal component basis (left) and the kernel-based discrepancy basis (right). The discrepancy uses independent copies of the kernel basis shown in the right-hand plot for the left and right streaks. Here  $p_\eta = 2$  and  $p_\delta = 2 \cdot 8$ .

### 3.4 Analysis and results

We model the simulation output using a principal component basis (Figure 15) derived from the 126 simulations over times ranging from 0 to  $12\mu\text{s}$ . The first two components account for over 99.9% of the variation. Hence we are satisfied that the choice of  $p_\eta = 2$  will give us sufficient accuracy for modeling the simulation output. Eight basis functions (also shown in Figure 15) are used to determine the discrepancy  $\boldsymbol{\delta}(x_1)$  as a function of time for each side of the cylinder expansion seen in the streak record. This allows for a smooth discrepancy over time in the simulated streak. The kernel width was chosen so that the resulting discrepancy term might be able to pick up genuine features of the expansion that the simulation model may not be able to account for, without picking up noise artifacts.

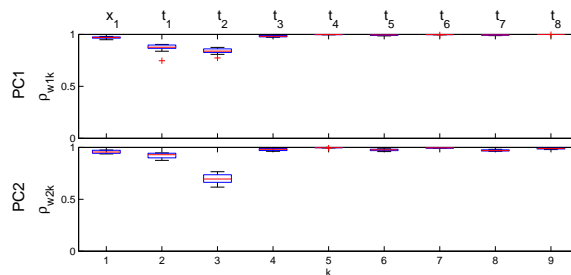


Figure 16: Boxplots of the marginal posterior distribution for each  $\rho_{wik}$ .

We first consider the fit to the simulation output, and then look at the inference using the experimental data as well. Boxplots of the marginal posterior distributions for the  $\rho_{wik}$ 's which govern the GP model for the simulator response are shown in Figure 16. In addition, Figure 17 shows the posterior mean of the simulator output  $\boldsymbol{\eta}(x_1, \boldsymbol{t})$  as one of the inputs is varied while the remaining inputs are held at their nominal value of 0.5. No effect for  $t_2$  (Gruneisen gamma) is

apparent in the 1-d effects of Figure 17. This is because the marginal effect of  $t_2$  is nearly 0. From looking at Figure 18, which shows the posterior mean surface for  $w_1(x_1, \mathbf{t})$ , it is clear that this parameter modifies the effect of  $t_1$  in the first PC; it is also clear that this effect, when averaged over  $t_1$ , or evaluated at  $t_1 = 0.5$  is 0.

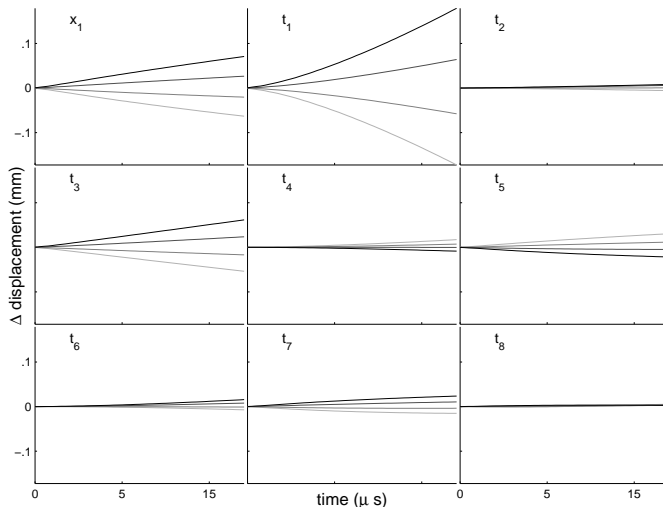


Figure 17: Estimated sensitivities of the simulator output from varying a single input while keeping the remaining eight inputs at their nominal value. The line shading corresponds to the input setting: light corresponds to low values; dark corresponds to high values.

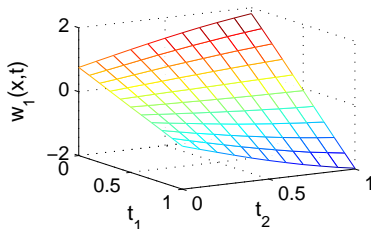


Figure 18: Posterior mean surface for  $w_1(x_1, \mathbf{t})$  where  $t_1$  and  $t_2$  vary across their prior ranges, while all other inputs are held at their nominal values of 0.5. This surface shows a clear interaction between the two inputs.

The simulation output is most strongly influenced by the density ( $x_1$ ), and three of the eight HE parameters ( $t_1$ ,  $t_2$  and  $t_3$ ). In addition,  $t_5$  and  $t_7$  have a very slight effect. Since the simulation output is nearly insensitive to parameters  $t_4$ ,  $t_6$  and  $t_8$ , we should expect the posterior distributions for these calibration parameters to be close to their uniform priors. It is tempting to conclude these parameters are unimportant for modeling this process. But one has to interpret carefully since the simulator is not reality.

The MCMC output resulting from sampling the posterior distribution of the full model (11) allows us to construct posterior realizations for the calibration parameters  $\boldsymbol{\theta}$ , the discrepancy process  $\boldsymbol{\delta}(x_1)$ , and predictions of the cylinder expansion at general input condition  $x_1$ . The estimated 2-dimensional marginal posterior distributions for  $\boldsymbol{\theta}$  are shown in Figure 19. The lines show estimated

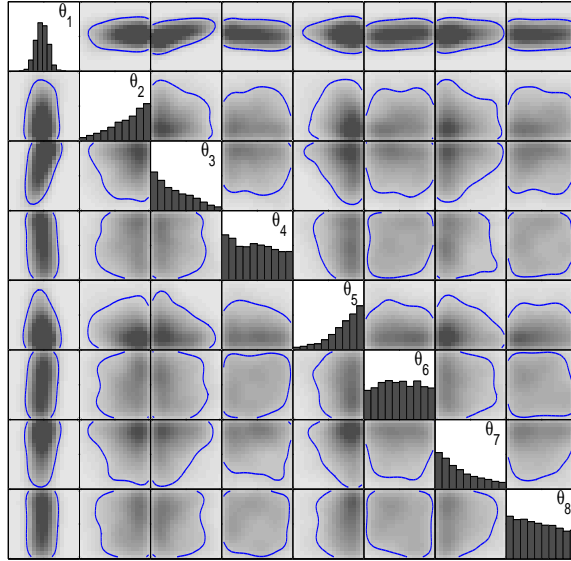


Figure 19: Two-dimensional marginals for the posterior distribution of the eight EOS parameters. The solid line gives the estimated 90% HPD region. The plotting regions correspond to the prior range of  $[0, 1]$  for each standardized parameter.

90% HPD regions for each margin. Recall the prior is uniform for each component of  $\theta$ . Not surprisingly, the most constrained parameter is  $\theta_1$ , the one that showed the strongest influence on the simulator output.

Figure 20 gives the posterior decomposition of the fitted value for the physical system  $\zeta(x_1)$  at  $x_1$ 's corresponding to the four experiments. The uncertainty in the posterior for  $\eta(x_1, \theta)$  is primarily due to uncertainty in  $\theta$ ; the uncertainty from the GP model for estimating  $\eta(x_1, t)$  in this example is negligible.

The posterior discrepancy is shown in the middle rows of Figure 20. Because two of the experiments are at the exact same condition  $x_1$  and the expansion streaks are recorded on two sides for three of the four experiments, the analysis has a fair bit of information to separate inadequacy of the simulation model from replicate variation. The curve of the fitted discrepancies highlights a consistent feature of the recorded streaks that is not explained by the model which gives much straighter streaks, regardless of the parameter setting. The exact cause of this curved discrepancy is believed to be due to insufficient flexibility in the EOS model.

Posterior predictions for the cylinder expansion  $\zeta(x_1)$  are given in the bottom row of Figure 20 for each of the experimental conditions. The curve in these predictions, due to the discrepancy model, more closely matches the experimental data as compared to those of the calibrated simulator only given in the top row.

The eventual goal is to combine *separate effects* tests like these HE cylinder experiments with *integrated effects tests* like the implosion experiments of Section 1.1 to better constrain unknown calibration parameters, and to improve prediction uncertainty in other integrated effects tests. It is in this context that we can judge the worth of this experiment. For example, the constraints on detonation energy obtained from this cylinder experiment might have helped us tease out the offsetting effects of detonation energy and yield stress of steel in the implosion application. Also,

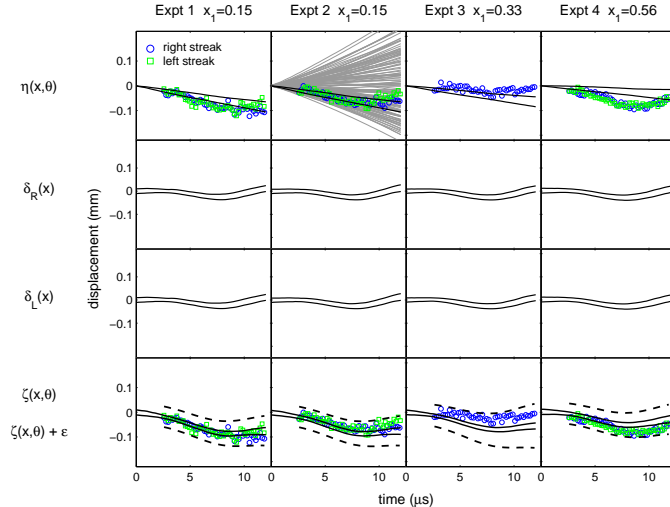


Figure 20: Posterior decomposition of the model fit for the cylinder expansion for each experiment. Top row: pointwise 90% credible intervals for the calibrated simulator  $\eta(x_1, \theta)$ ; middle rows: pointwise 90% credible intervals for the discrepancy terms corresponding to the right and left camera streaks  $\delta_R(x_1)$  and  $\delta_L(x_1)$ ; bottom row pointwise 90% credible intervals for prediction of the physical system  $\zeta(x_1) = \eta(x_1, \theta) + \delta(x_1)$  (solid lines) and for a new experiment  $\zeta(x_1) + \epsilon$  (dashed lines). Also shown in the top and bottom rows are the data from the streak camera from each of the experiments. The gray lines show the 126 simulated traces.

how much one should worry about detected inadequacy in a simulation model can also be evaluated in a similar light. For example if the discrepancy observed in the HE cylinder experiments causes concern in our ability to adequately model an implosion, then perhaps more effort on improved EOS models is called for, rather than more experiments.

## 4 Discussion

The modeling approach described in this paper has proven quite useful in a number of applications at LANL. Application areas include shock physics, materials science, engineering, cosmology, and particle physics.

The success of this approach depends, in large part, on whether or not the simulator can be efficiently represented with the GP model on the basis weights  $w_i(\mathbf{x}, \mathbf{t})$ ,  $i = 1, \dots, p_\eta$ . This is generally the case for highly forced systems—such as an implosion—which are dominated by a small number of modes of action. This is apparent in the principal component decomposition, which partitions nearly all of the variance in the first few components. These systems also tend to exhibit smooth dependence on the input settings. In contrast, more chaotic systems seem to be far less amenable to a low-dimensional description such as the PC-basis representations used here. Also, system sensitivity to even small input perturbations can look almost random, making it difficult to construct a statistical model to predict at untried input settings. We therefore expect that an alternative approach is required for representing the simulator of a less forced, more chaotic system.

Finally, we note that the basic framework described here does lead to issues that require careful consideration. The first is the interplay between the discrepancy term  $\delta(\mathbf{x})$  and the calibration parameters  $\theta$ ; this is noted in the discussion of Kennedy and O’Hagan (2001), as well as in a number of other articles (Higdon et al., 2004; Bayarri et al., 2002; Loepky et al., 2005) The basic point here is that if substantial discrepancy is present, then its form will affect the posterior distribution of the calibration parameters. The second is the issue of extrapolating outside the range of experimental data. The quality of such extrapolative predictions depends largely on the trust one has for the discrepancy term  $\delta(\mathbf{x})$ —is what is learned about the discrepancy term at tried experimental conditions  $\mathbf{x}_1, \dots, \mathbf{x}_n$  applicable to a new, possibly far away, condition  $\mathbf{x}^*$ ? Third, and last, we note that applications involving a number of related simulation models require additional modeling considerations to account for the relationship between the various simulation models. See Kennedy and O’Hagan (2000) and Goldstein and Rougier (2005) for examples.

## References

- Bayarri, M., Berger, J., Higdon, D., Kennedy, M., Kottas, A., Paulo, R., Sacks, J., Cafeo, J., Cavendish, J. and Tu, J. (2002). A framework for the validation of computer models, *in* D. Pace and S. Stevenson (eds), *Proceedings of the Workshop on Foundations for V&V in the 21st Century*, Society for Modeling and Simulation International, pp. ?–?
- Bayarri, M. J., Berger, J. O., Paulo, R., Sacks, J., Cafeo, J. A., Cavendish, J., Lin, C. H. and Tu, J. (2005). A framework for validation of computer models, *Technical report*, Statistical and Applied Mathematical Sciences Institute.
- Bengtsson, T., Snyder, C. and Nychka, D. (2003). Toward a nonlinear ensemble filter for high-dimensional systems, *Journal of Geophysical Research* **108**: 1–10.
- Berliner, L. M. (2001). Monte Carlo based ensemble forecasting, *Statistics and Computing* **11**: 269–275.
- Besag, J., Green, P. J., Higdon, D. M. and Mengersen, K. (1995). Bayesian computation and stochastic systems (with discussion), *Statistical Science* **10**: 3–66.
- Goldstein, M. and Rougier, J. C. (2005). Probabilistic formulations for transferring inferences from mathematical models to physical systems, *SIAM Journal on Scientific Computing* **26**: 467–487.
- Hastings, W. K. (1970). Monte Carlo sampling methods using Markov chains and their applications, *Biometrika* **57**: 97–109.
- Higdon, D. (1998). A process-convolution approach to modeling temperatures in the north Atlantic Ocean, *Journal of Environmental and Ecological Statistics* **5**: 173–190.
- Higdon, D., Kennedy, M., Cavendish, J., Cafeo, J. and Ryne, R. D. (2004). Combining field observations and simulations for calibration and prediction, *SIAM Journal of Scientific Computing* **26**: 448–466.
- Higdon, D. M., Lee, H. and Holloman, C. (2003). Markov chain Monte Carlo-based approaches for inference in computationally intensive inverse problems, *in* J. M. Bernardo, M. J. Bayarri, J. O. Berger, A. P. Dawid, D. Heckerman, A. F. M. Smith and M. West (eds), *Bayesian Statistics 7. Proceedings of the Seventh Valencia International Meeting*, Oxford University Press, pp. 181–197.
- Kaipio, J. P. and Somersalo, E. (2004). *Statistical and Computational Inverse Problems*, Springer, New York.
- Kao, J., Flicker, D., Ide, K. and Ghil, M. (2004). Estimating model parameters for an impact-produced shock-wave simulation: optimal use of partial data with the extended Kalman filter, *Journal of Computational Physics* **196**: 705–723.

- Kennedy, M. and O'Hagan, A. (2000). Predicting the output from a complex computer code when fast approximations are available, *Biometrika* **87**: 1–13.
- Kennedy, M. and O'Hagan, A. (2001). Bayesian calibration of computer models (with discussion), *Journal of the Royal Statistical Society (Series B)* **68**: 425–464.
- Kern, J. (2000). Bayesian process-convolution approaches to specifying spatial dependence structure, Ph.D. Thesis, Institute of Statistics and Decision Sciences, Duke University.
- Leary, S., Bhaskar, A. and Keane, A. (2003). Optimal orthogonal-array-based Latin hypercubes, *Journal of Applied Statistics* **30**: 585–598.
- Linkletter, C., Bingham, D., Hengartner, N., Higdon, D. and Ye, K. (2006). Variable selection for Gaussian process models in computer experiments, *Technometrics* **48**: 478–490.
- Loeppky, J., Bingham, D., Sacks, J. and Welch, W. J. (2005). Biased estimation of calibration and tuning parameters in a possibly biased computer model, *Technical report*, University of British Columbia.
- Metropolis, N., Rosenbluth, A., Rosenbluth, M., Teller, A. and Teller, E. (1953). Equations of state calculations by fast computing machines, *Journal of Chemical Physics* **21**: 1087–1091.
- Neddermeyer, S. (1943). Collapse of hollow steel cylinders by high explosives, *Los Alamos Report LAR-18*, Los Alamos National Laboratory.
- Oakley, J. and O'Hagan, A. (2004). Probabilistic sensitivity analysis of complex models, *Journal of the Royal Statistical Society (Series B)* **66**: 751–769.
- O'Hagan, A. (1978). Curve fitting and optimal design for prediction, *Journal of the Royal Statistical Society (Series B)* **40**: 1–24.
- Ramsay, J. O. and Silverman, B. W. (1997). *Functional Data Analysis*, Springer, New York.
- Sacks, J., Welch, W. J., Mitchell, T. J. and Wynn, H. P. (1989). Design and analysis of computer experiments (with discussion), *Statistical Science* **4**: 409–423.
- Santner, T. J., Williams, B. J. and Notz, W. I. (2003). *Design and analysis of computer experiments*, Springer, New York.
- Tang, B. (1993). Orthogonal array-based Latin hypercubes, *Journal of the American Statistical Association* **88**: 1392–1397.
- Williams, B., Higdon, D., Gattiker, J., Moore, L., McKay, M. and Keller-McNulty, S. (2006). Combining experimental data and computer simulations, with an application to flyer plate experiments, *Bayesian Analysis* **1**: 765–792.
- Ye, K. Q., Li, W. and Sudjianto, A. (2000). Algorithmic construction of optimal symmetric Latin hypercube designs, *Journal of Statistical Planning and Inference* **90**(1): 145–159.